Pulsed Laser Ablation of Dental Calculus in the Near-Ultraviolet

Introduction

Selective removal of subgingival dental calculus is a preferred treatment method in nonsurgical periodontal therapy. While complete removal of calculus and disease-causing agents (i.e., oral bacteria) is of primary importance, leaving behind a hard tissue surface less prone to bacterial accumulation is also important. Grooves and craters resulting from conventional cleaning measures provide sites for future bacteria and calculus crystals to accumulate.[1] Healthy cementum should be preserved since attachments, via periodontal ligaments, from either the gingiva or alveolar bone with root dentin are not as strong as with root cementum.[2,3] A weak connection could lead to subsequent reoccurrence of periodontal problems.

Conventional methods to remove calculus typically depend on the experience of the clinician[4,5] and other treatment factors.[1] Unintentional damage can easily occur using hand instruments[6] and power-driven scalers (e.g., ultrasonic and air abrasion)[7] that cause grooves and/or excessive cementum removal. In most cases, mechanical root scaling leaves behind a smear layer containing harmful bacteria, infected cementum, and calculus debris.[8,9]

Currently, the Er:YAG laser ($\lambda = 2.94$ μm) (Ref. 10) is the only commercially available laser with significant experimental and clinical studies for dental hard tissue removal.[1] Hard-tissue (enamel, dentin, and cementum) ablation at this wavelength relies on absorption by water,[11] so calculus ablation is not selective. A review of several clinical studies[12] and recent meta-analysis[13] concluded that the clinical outcome of calculus removal using the Er:YAG laser is similar to conventional mechanical debridement.

A frequency-doubled alexandrite (FDA) laser ($\lambda \sim 380$ nm) can selectively remove plaque, caries, and calculus without damaging the underlying and surrounding hard tissue.[14] The ablation mechanism is assumed to be based on absorption by haemins (i.e., iron-containing porphyrins) into the Soret band.[15,16] Iron-containing porphyrins are found in some oral bacteria in dental plaque and dental calculus.[15,17] However, the inconsistent output of the FDA laser has not allowed for more-detailed studies into the calculus ablation mechanism.

Recently, a frequency-doubled Ti:sapphire laser ($\lambda = 400$ nm) was developed to allow for a more-detailed analysis of dental calculus ablation in the near-ultraviolet (NUV, 300 to 400 nm) (Ref. 18). This laser selectively removes dental calculus[19,20] and extrinsic enamel stains.[21] For incident laser fluences close to the ablation threshold (1 to 2 J/cm^2), ablation stalling is frequently encountered. Stalling is not observed at fluences well above the ablation threshold (6 to 8 J/cm^2).

This article describes a variety of experimental diagnostics used to study the ablation mechanism of dental calculus at 400 nm and compares the results with predictions made by heuristic ablation models. Laser profilometry measures volume and depth of calculus ablated for different irradiation conditions. Blue-light microscopy and fluorescence spectroscopy identify photobleaching during calculus ablation. Together these diagnostics allow one to identify a heuristic, modified ablation blowoff model that explains the experimental observations. Finally, the effect of tooth sterilization prior to laser irradiation is assessed by comparing removal rates of gamma-ray–sterilized and unsterilized calculus samples at the same incident fluence. This information has been used to propose a mechanism for calculus ablation at 400 nm.

Heuristic Ablation Models

1. Standard Blowoff Model

In the standard blowoff model, Beer's law is assumed to govern energy deposition into calculus.[22] In this model, deposited energy densities E_d exceeding the ablation-threshold energy density E_{abl} cause calculus removal. The threshold energy density is typically a constant[22,23] related to the enthalpy of ablation for calculus. The absorption coefficient μ_a is assumed to remain constant during irradiation, and scattering is assumed to be negligible. For the standard blowoff model, E_d is given by

$$E_d = -\frac{dF}{dz} = \mu_a F(z) = \mu_a F_0 e^{-\mu_a z}, \qquad (1)$$

where F_0 is the incident fluence (in J/cm^2) and $F(z)$ is the fluence at depth z. Ablation occurs over the etch depth δ_{SB} if $\mu_a F(z) > E_{abl}$. Beyond the etch depth, tissue is not ablated but merely heated. The fluence at the etch depth is the ablation threshold fluence F_{th}, and for $F(z) > F_{th}$ the etch depth is found from Eq. (1) to be

$$\delta_{SB} = \frac{1}{\mu_a} \ln\left(\frac{F_0}{F_{th}}\right). \tag{2}$$

2. Modified Blowoff Model

In the modified blowoff model, the absorption coefficient is assumed to decrease during the laser pulse. This assumption may be better suited for predicting calculus-removal rates since a photobleached surface layer is observed after 400-nm irradiation.[18] This model was originally proposed for photoablation of polymethyl methacrylate (PMMA) in the deep ultraviolet.[23] For photoablation, the number density of chromophores ρ_a decreases as the absorption of UV photons breaks chemical bonds that prevent absorption of subsequent photons.[24,25] Permanent photochemical damage of the chromophores (i.e., photobleaching) similarly decreases ρ_a during laser irradiation. The derivation for the modified blowoff model is found in Ref. 23, where the approximate etch depth δ_{MB}, for the fluences used in this article, is determined to be

$$\delta_{MB} \approx \frac{F_0 - F_{th}}{h\nu\rho_a}, \tag{3}$$

where h is Planck's constant and ν is the laser frequency. The etch depth depends linearly on F_0 as opposed to the logarithmic dependence in Eq. (2) for the standard model. The full expression for Eq. (3) is found in Ref. 23. The chromophore number density is related to the absorption coefficient by $\mu_a = \sigma_a\rho_a$, where σ_a is the absorption cross section of the chromophore. The deposited energy density is approximately constant for $z < \delta_{MB}$ and is given by

$$E_d\left(z < \delta_{MB}\right) \approx h\nu\rho_a. \tag{4}$$

Equation (4) indicates that the deposited energy is limited by the chromophore number density of the tissue within the etch depth. The deposited energy density for both blowoff models is plotted as a function of depth in Fig. 134.53 based on the data in Table 134.VI. A layer consisting of partially photobleached chromophores is located beyond the etch depth in Fig. 134.53(b).
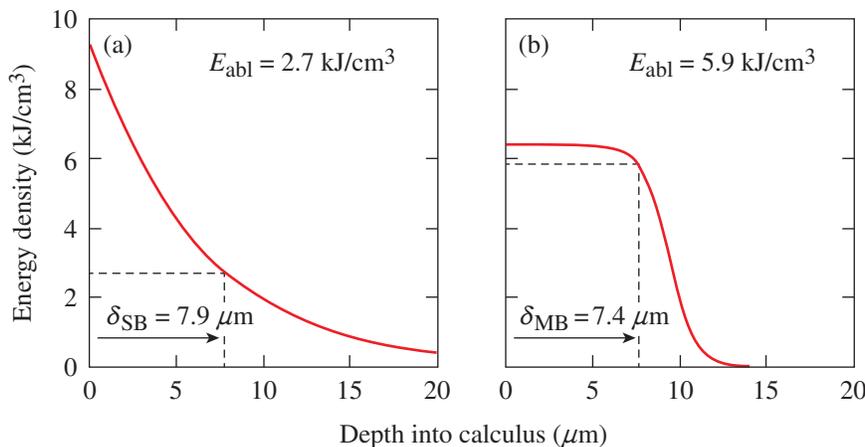

E21791JR

Figure 134.53
Deposited energy density as a function of depth in calculus based on the (a) standard and (b) modified blowoff models. The incident fluence is 6 J/cm^2. The curves are based on data in Table 134.VI. In (a) $\mu_a = 1600$ cm^{-1} and in (b) $\rho_a = 1.3 \times 10^{22}$ cm^{-3}.

Table 134.VI: Absorption coefficients, threshold fluences, and chromophore number densities for the standard and modified blowoff models obtained from removal rates in Fig. 134.58.

	Removal Rates		Standard Blowoff Model		Modified Blowoff Model	
	$\dfrac{\mu\text{m/pulse}}{\text{J/cm}^2}$	$\times 10^{14} \dfrac{\mu\text{m}^3/\text{pulse}}{\text{J/cm}^2}$	μ_a (cm^{-1})	F_{th} (J/cm^2)	ρ_a 10^{22} (cm^{-3})	F_{th} (J/cm^2)
Supragingival	1.5±0.3	6.6±1.4	1618±323	1.7±0.4	1.32±0.27	1.2±0.4
Subgingival	1.6±0.3	7.9±1.6	1574±281	1.8±0.4	1.27±0.23	1.3±0.4

3. Removal Rates

The etch depths in Eqs. (2) and (3) can be used to calculate volume removal rates for each blowoff model. Assuming an nth-order super-Gaussian fluence distribution $F(r)$, we find

$$F(r) = F_0 \exp\left(-r^n / w^n\right), \tag{5}$$

with peak fluence F_0 and $1/e$ beam width w. Substituting Eq. (5) into Eqs. (2) and (3), one obtains a radial distribution of the etch region. Scattering is assumed to be negligible compared to absorption. The volume removal rate is found by integrating over the entire volume irradiated at fluences $>F_{th}$. The volume removal rate V_{SB} per pulse for the standard blowoff model is

$$V_{SB} = \frac{2\pi w^2}{\mu_a}\left(\frac{1}{n+2}\right)\left(\ln\frac{F_0}{F_{th}}\right)^{\frac{n+2}{n}}. \tag{6}$$

The volume removal rate predicted by the modified blowoff model V_{MB} is

$$V_{MB} = \frac{2\pi^2}{\rho_a h\nu}\left[\frac{F_0\Gamma(2/n)}{n}\eta_E\left(n, F_0/F_{th}\right) - \frac{F_{th}}{2}\left(\ln\frac{F_0}{F_{th}}\right)^{2/n}\right], \tag{7}$$

where η_E is the energy efficiency for selective ablation shown in Ref. 18 and Γ is the gamma function. For our experimental conditions the volume removal rates in Eqs. (6) and (7) simplify to $V_{SB}(\mu m^3) \approx (10^8/\mu_a)$ and $V_{MB}(\mu m^3) \approx (F_0/\rho_a) \times 10^{27}$, where the units of ρ_a, μ_a, and F_0 are cm^{-3}, cm^{-1}, and J/cm^2, respectively. The underlying experimental parameters are $n = 10$, $w = 150\,\mu m$, $F_0/F_{th} \approx 4$ to 5, $\eta_E \approx 1$, and $h\nu = 3.1$ eV.

Materials and Methods

1. Tooth Samples

Twenty extracted human teeth exhibiting calculus, equally divided between sub- and supragingival calculus, were obtained from the Department of Preventive and Restorative Dental Sciences, School of Dentistry at the University of California, San Francisco. They were sterilized with gamma radiation and stored in a 0.1% thymol solution. Ten extracted, unsterilized human teeth with subgingival calculus were obtained from the Eastman Institute for Oral Health at the University of Rochester (UR) and stored in a saline solution.

2. Experimental Setup

A frequency-doubled Ti:sapphire laser (400-nm wavelength, 60-ns pulse duration, 10-Hz repetition rate, and 25-mJ pulse energy) was developed for selective calculus ablation and has been described elsewhere.[18] Laser radiation was coupled into a 600-μm-core-diam optical fiber with a 1.8-mm-diam tapered input (FVPE600660710/2M, Polymicro Technologies) using a $\Delta\theta = 0.5°$ engineered diffuser (RPC Photonics) and an $F = 7.5$-cm lens [Fig. 134.54(a)]. The output beam was demagnified using an $F = 2$-cm lens objective to create an $\sim$300-μm-diam, tenth-order super-Gaussian irradiation beam on the calculus surface. This irradiation geometry was chosen to facilitate experimental observations. The peak fluence of each pulse was varied from 1.7 to 8 J/cm^2 ($\pm$0.1 J/cm^2) by varying the laser pulse energy. All tooth surfaces were irradiated at normal (perpendicular) incidence to the surface. (Similar ablation studies using oblique incidence were reported in Ref. 19.)

During laser irradiation, the tooth samples were sprayed with a water/air mixture at $\sim$3 mL/min. The effect of this water spray on the intensity distribution of the irradiation laser at the tooth surface is minimal.[18] After five laser pulses, excess water was gently blown off the tooth samples using an air spray to allow for the diagnostic imaging (i.e., laser profilometry and blue-light microscopy) described below.

3. Laser Profilometry

The depth and volume of calculus removed were measured using a laser profilometer. A HeNe laser at $\lambda = 543$ nm (Model LHGR-0050, PMS Electro-Optics) was focused to a line onto the tooth surface using an $F = 10$-cm cylindrical lens and then scanned across the irradiated region before and after laser irradiation. The line was magnified 3$\times$ (VMZ450i, Edmund Industrial Optics) by imaging onto a charge-coupled–device (CCD) camera (TM-1020A-15CL, JAI) along a line of sight at 45°, resulting in an axial resolution of $\sim$6 μm. The transverse resolution was 60 μm $\times$ 40 μm. Depth-removal maps were found by taking the difference between 3-D surface images taken before and after irradiation (as described in Ref. 19). Calculus removal rates were determined by irradiating in five-pulse increments using a remotely operated shutter in the laser cavity. The average depth and volumetric removal rate uncertainties are $\pm$0.6 μm/pulse and 1.4 $\times$ 10^{-3} μm^3/pulse based on the uncertainty in the 3-D surface images resulting from laser speckle and the high f number of the imaging objective.

4. Blue-Light Microscopy

Images of calculus before and after laser irradiation were taken with illumination from a flashing blue light–emitting diode (LED, $\lambda \sim 450$ to 490 nm) using the same camera used in laser profilometry, as shown in Fig. 134.54(a). Identical images were obtained when illuminating with a 400-nm light source. Blue-light illumination provides high contrast between healthy
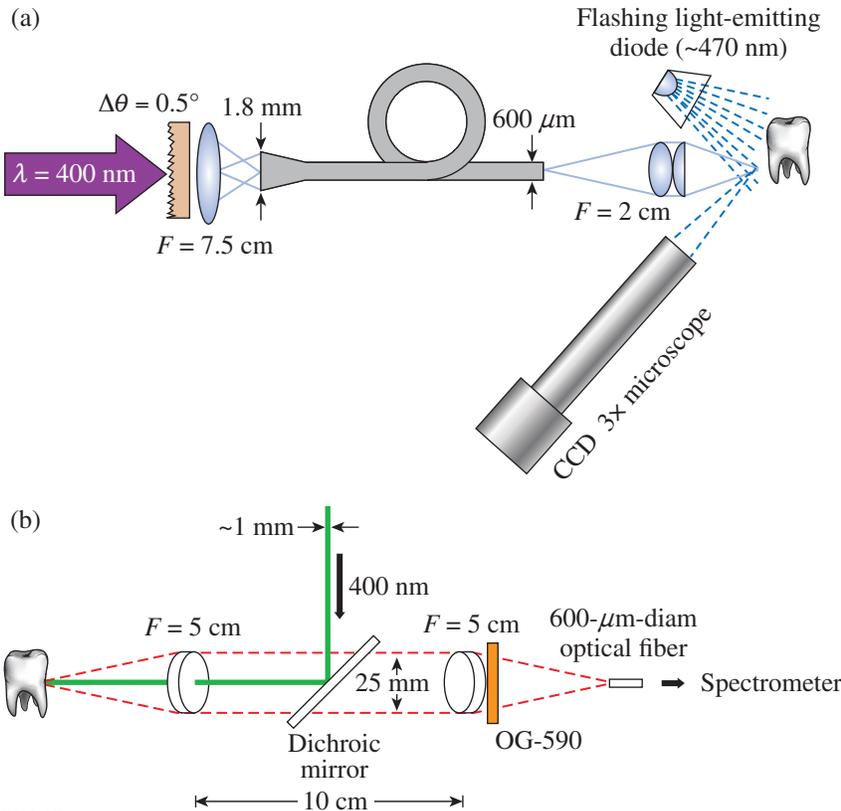
(a)

(b)

Figure 134.54
(a) Experimental setup for tooth irradiation with the 400-nm laser and for blue-light microscopy. (b) Hard tissue fluorescence between 600 and 800 nm was excited at 400 nm and coupled into an optical fiber leading to a fiber-coupled spectrometer. CCD: charge-coupled device.

E21792JR

hard tissue and dental calculus. It also serves to qualitatively distinguish unbleached from photobleached calculus since the latter appears brighter under blue-light microscopy because of increased scattering and decreased absorption.

5. Fluorescence Spectroscopy

Fluorescence spectroscopy was used to compare unbleached and photobleached calculus. As shown in Fig. 134.54(b), fluorescence was excited with low pulse energy (≤ 200 μJ at 400 nm) over a 50-μm beam spot. Fluorescence between 600 and 800 nm was then directed into a fiber-coupled spectrometer (HR2000CG-UVNI, Ocean Optics) using two $F = 5$-cm achromatic doublets, a dichroic mirror, and an OG590 filter. In this spectral range, one can discriminate between dental hard tissue and calculus caused by fluorescence from bacterial porphyrins.[26] At each measurement, 50 spectra were collected with a 10-s integration time, averaged, and smoothed by applying an ~5-nm spectral averaging filter.

6. Scanning Electron Microscopy

The laser-treated areas were examined using a scanning electron microscope (SEM) (Zeiss-Auriga CrossBeam FIB-SEM, Carl Zeiss NTS) at the UR's Institute of Optics. The tooth surface topology was examined using an SE2 detector and a 10-keV electron beam with a 30-μm aperture and ≤ 15-mm working distance. The teeth were dried in a desiccator for at least 24 h. An ~5-nm gold layer was subsequently sputtered onto the tooth surface.

Results

Blue-light microscope images show nonsterilized subgingival calculus removed at 6.4 J/cm^2 [Figs. 134.55(a)–134.55(f)] within the irradiation beam (dashed red lines). After 30 pulses, the calculus was completely removed and the underlying cementum was reached [Fig. 134.55(f)]. No ablative stalling was observed, but irradiated calculus appears brighter compared to nonirradiated calculus, indicating a photobleached surface layer. Differential depth removal maps [Figs. 134.55(g)–134.55(k)] are shown below the microscope images. Average depth and volume removal rates for nonsterilized calculus are 9.7±3.1 μm/pulse and 5.3 × 10^5±1.8 × 10^5 μm^3/pulse, respectively. Identical results are found for ablating sterilized subgingival calculus[19] at the same fluence.

Blue-light microscope and fluorescence spectra of supragingival calculus irradiated at a 3.5-J/cm^2 fluence are shown in Figs. 134.56(a) and 134.56(b). The calculus was irradiated with a 650-μm-diam, sixth-order super-Gaussian beam. The tooth
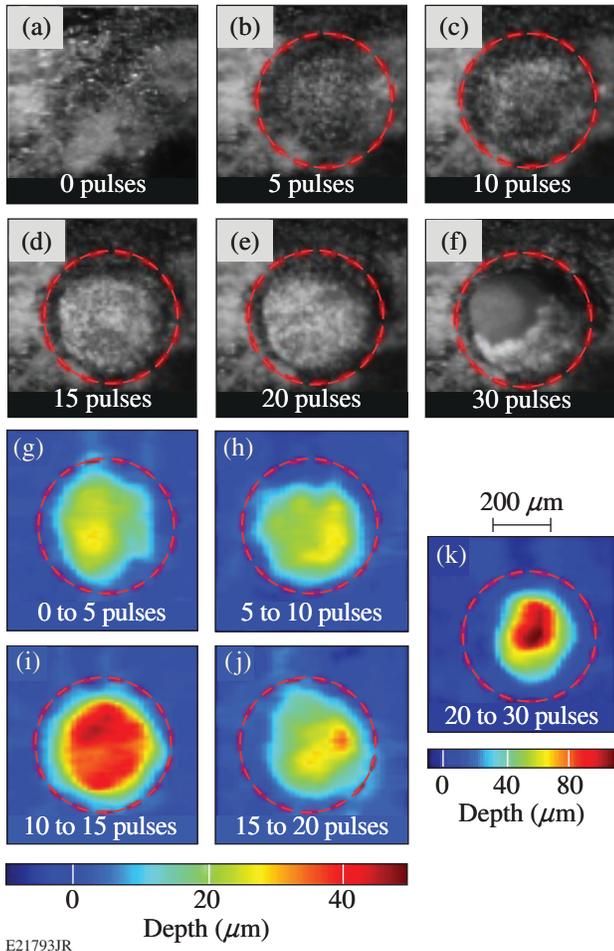
Figure 134.55
Blue-light microscope images of nonsterilized subgingival calculus irradiated at 6.4 J/cm^2 (a) before and after (b) 5, (c) 10, (d) 15, (e) 20, and (f) 30 irradiation pulses. Differential removal maps from (g) 0 to 5, (h) 5 to 10, (i) 10 to 15, (j) 15 to 20 and (k) 20 to 30 irradiation pulses correspond to the above microscope images. Red dashed circles outline the irradiation area.

was moved back and forth for 40 passes at 0.2 mm/s, resulting in ~30 superposed irradiation pulses per pass along the center on any given spot. The blue-light microscope images before and after irradiation [Figs. 134.56(a) and 134.56(b)] indicate that a layer of calculus was removed but a photobleached calculus surface layer remained [blue arrow in Fig. 134.56(b)]. The ablation stalled and further irradiation at this fluence removed no additional calculus.

Figure 134.56(c) shows the fluorescence spectra between 600 and 800 nm, excited at 400 nm, of the enamel (black arrow), unbleached calculus (red arrow), and photobleached calculus (blue arrow) indicated in Fig. 134.56(b). The fluorescence spectrum of photobleached calculus resembles the spectrum of enamel in shape, emitting more fluorescence photons

than unbleached calculus [Fig. 134.56(c)]. Normalizing each spectrum [Fig. 134.56(d)] reveals that unbleached calculus has a distinct structure between 615 and 725 nm caused by the Soret band of porphyrins.[26–28] This band is not seen for either enamel or photobleached calculus. Fluorescence from these tissues originates from the hard-tissue matrix. Remnant unbleached porphyrins within the photobleached calculus likely result in the differences observed for enamel and photobleached calculus spectra.

Removing the OG590 filter in the fluorescence setup allowed us to measure the scattered/reflected signal at 400 nm. Photobleached calculus and enamel scattered twice as much 400-nm light into the collection optics as did unbleached calculus. The exact amount of 400-nm light scattered by photobleached calculus varies from tooth to tooth and can equal that for sound enamel.

Subgingival calculus irradiated with 25 pulses at 5 J/cm^2 was investigated under a SEM [Fig. 134.57(a)]. The ~100-nm pores on the calculus surface [arrows in Fig. 134.57(a)] act as
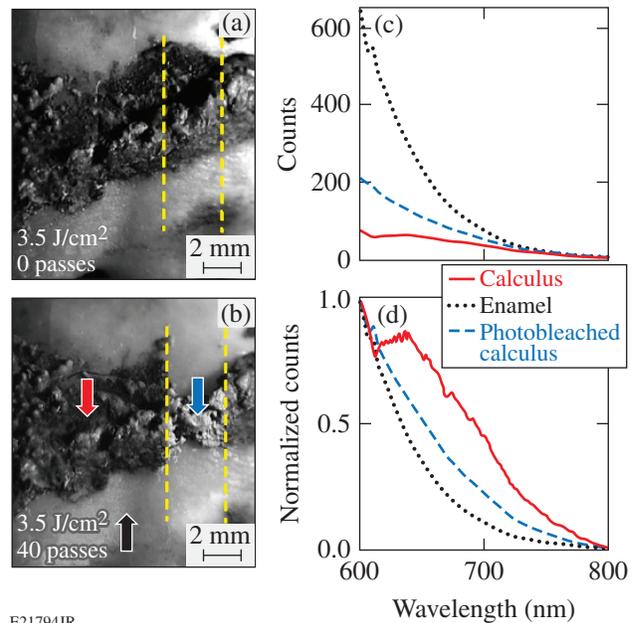
Figure 134.56
Blue-light microscope images of supragingival calculus on enamel (a) before and (b) after 40 passes at 3.5 J/cm^2 using an ~650-μm-diam, sixth-order super-Gaussian beam. The dashed yellow lines outline the irradiation path. (c) Fluorescence spectra of enamel, unbleached calculus, and photobleached calculus using a 400-nm excitation wavelength. (d) Normalized fluorescence spectra corresponding to (c). Colored arrows in (b) correspond to the spectra in (c) and (d) (i.e., red arrow: unbleached calculus; black arrow: enamel; and blue arrow: photobleached calculus).

a reservoir for oral bacteria.[29–32] For comparison, the porous surface of non-laser-irradiated calculus, covered with a biofilm, was also observed under a SEM [Fig. 134.57(b)]. The calculus surface was always covered by a layer of noncalcified dental plaque.[1] Blue-light microscope images (not shown) of the irradiated calculus surface in Fig. 134.57(a) indicate it was photobleached. The pores seen in this image were likely originally filled with oral bacteria that were removed upon NUV irradiation.

Average depth and volume removal rates for sub- and supragingival calculus are plotted as a function of incident fluence in Fig. 134.58. Within the error bars, both depth and volume removal rates increase linearly with increasing incident fluence and are indistinguishable between sub- and supragingival calculus. We have attributed the large error bars to tissue variations in absorption and/or the heterogeneity of the physical properties in calculus.[19] The absolute error in depth and volume removal rates increases with fluence in Fig. 134.58 but the relative error actually decreases. Depth removal rates in Figs. 134.58(a) and

134.58(b) are fitted to Eqs. (2) and (3). The results from these fits are summarized in Table 134 VI. The error bars render μ_a, ρ_a, and F_{th} indistinguishable for both types of calculus. The relevant tissue parameters in Table 134 VI are substituted into Eqs. (6) and (7) and plotted in Figs. 134.58(c) and 134.58(d) as predicted volume removal rates for sub- and supragingival calculus, respectively. The modified blowoff model overestimates the volume removal rate, whereas the standard model underestimates it.

The single-pulse (SP) depth and volume removal rates at ~6.3 J/cm^2 for either subgingival [Figs. 134.59(a) and 134.59(c)] or supragingival [Figs. 134.59(b) and 134.59(d)] calculus show similar trends with the number of incident pulses. The SP removal rate is calculated as the depth/volume removed from five laser pulses divided by the number of pulses, whereas the average removal rates in Fig. 134.58 are calculated from the total depth/volume removed. Outliers in the SP removal-rate data that skew the distribution are rejected according to Chauvenet's criterion.[33] The SP removal rates of sub- and
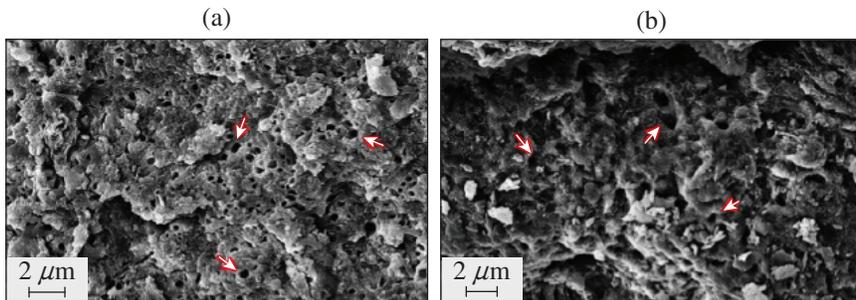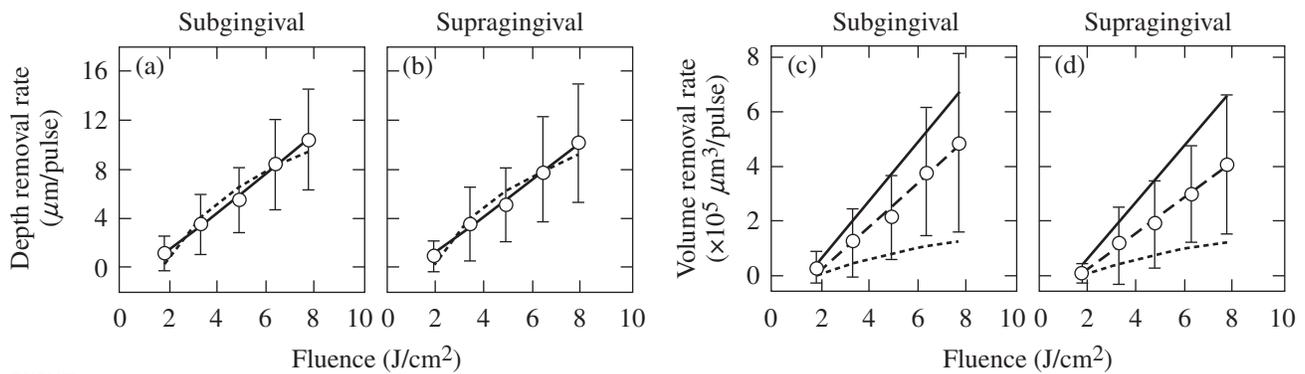

(a)   (b)

Figure 134.57
Scanning electron microscope (SEM) images of (a) laser-irradiated (5-J/cm^2) and (b) non-laser-irradiated subgingival calculus. Arrows in (a) and (b) indicate representative ~100-nm craters found in the calculus surface.

E21795JR

E21796JR

Figure 134.58
Fluence-dependent depth removal rates for (a) subgingival and (b) supragingival calculus and corresponding volume removal rates [(c) and (d), respectively]. Solid and short-dashed lines correspond to fits using the modified and standard blowoff models, respectively. Long-dashed lines in (c) and (d) are a linear regression through the data.
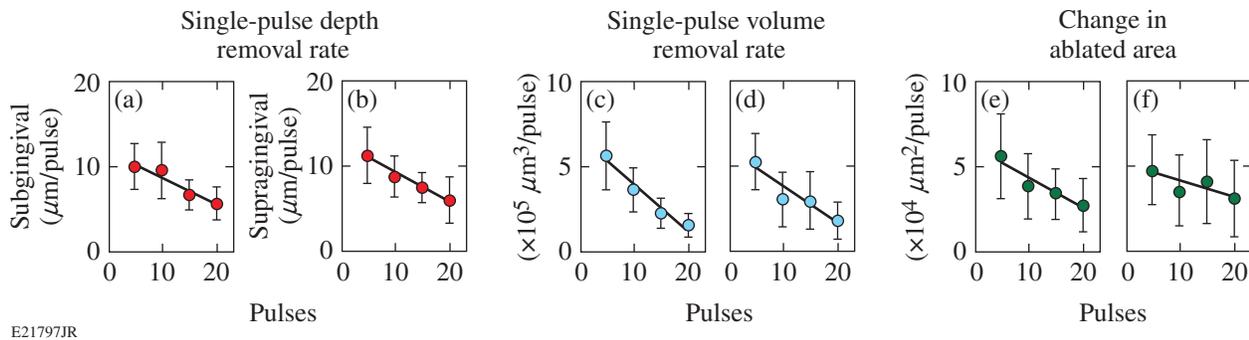
E21797JR

Figure 134.59

Single-pulse (SP) removal rates for all calculus samples irradiated at 6.3 J/cm^2 as a function of the number of incident pulses: the SP depth removal rates for (a) subgingival and (b) supragingival calculus; the SP volume removal rates for (c) subgingival and (d) supragingival calculus; the change in ablated area for (e) subgingival and (f) supragingival calculus. Trend lines through data are from a linear regression.

supragingival calculus at fluences from 3.5 to 7.7 J/cm^2 exhibit similar behavior. The change in the ablated area at 6.3 J/cm^2 for sub- and supragingival calculus [Figs. 134.59(e) and 134.59(f)] was found by dividing the SP volume removal rates by the SP depth removal rates in Fig. 134.59. The ablated area also decreases with increasing number of incident pulses. There is no statistically significant difference between the SP removal rates for sub- and supragingival calculus.

Discussion

The properties (i.e., pulse energy and duration) of the 400-nm laser used in this study are extremely reproducible, causing shot-to-shot variations in ablation measurements to be attributable to the material heterogeneity of calculus itself. Therefore, using the diagnostics outlined earlier allows for rather detailed inferences regarding the actual ablation mechanism. This contrasts with previous work using the 380-nm FDA laser[34] whose poor reproducibility and characterization rendered it unsuitable for this kind of detailed study. However, the selective removal of oral bacteria, dental caries, and calculus by the 380-nm laser (summarized in Ref. 14) was attributed to porphyrins endogenous to oral bacteria.

In this study, blue-light microscopy clearly indicates photobleaching and reduced absorption on the calculus surface after laser irradiation (Figs. 134.55 and 134.56). For thick calculus layers and laser fluences of less than ~6 J/cm^2, this may lead to stalling before the entire calculus layer is removed. Therefore, photobleaching affects calculus ablation but does not necessarily prevent it.

Fluorescence spectroscopy (Fig. 134.56) supports the interpretation of the blue-light microscope images. The fluorescence spectra [Fig. 134.56(c)] of irradiated and nonirradi-

ated photobleached calculus show that endogenous porphyrins (e.g., protoporphyrin IX and coporphyrin) in oral bacteria (e.g., *P. intermedia*, *P. nigrescens*, and *P. melaninogenica*) are the primary absorbers for 400-nm ablation. This finding is further supported by the corresponding SEM images in Fig. 134.57, which show empty pores and paucity of microorganisms on the surface of irradiated calculus. These diagnostics are unable to determine, however, the depth of this photobleached layer, which, from here on, we refer to as the "depletion layer." This depletion layer also leads to the measured increase in reflection/scattering of 400-nm radiation compared to nonirradiated calculus and clearly affects ablation by subsequent laser pulses.

The modified blowoff model appears well suited to explain calculus ablation at 400 nm, while the standard blowoff model does not. The assumption of permanent chromophore depletion agrees with the results of blue-light microscopy, fluorescence spectroscopy, and scattered-laser-light measurements. The model predicts a partially depleted layer of chromophores [Fig. 134.55(b)] with thickness ~1/μ_a beyond the etch depth after each laser pulse. The linear dependence of the average depth and volume removal rates with incident fluence (Fig. 134.57) also agrees with this model.

The modified blowoff model readily agrees with most of the observations in Figs. 134.55–134.58. This model does not, however, predict the ablation stalling seen in Fig. 134.56 nor the reduction of ablation depth and volume with successive laser pulses in Fig. 134.59. This limitation probably is caused mostly by the modified blowoff model neglecting scattering of laser light within dental calculus. These losses, especially within the depletion layer, can be significant because of multiple scattering, including broadening of the spot size. In addition, calculus formation is layered,[35] progressing from low chromo-

phore number density (low ρ_a), gram-positive bacteria[36] on the calculus/tooth interface to high ρ_a, gram-negative bacteria on the calculus surface.[36–40]

The gradual decrease in absorber density with depth and the concomitant increase in the depletion layer exacerbate the laser-light losses ahead of the region where it may be effectively absorbed. This naturally leads to decreasing removal rates with depth (Fig. 134.59) and potential stalling. This problem is compounded by the fact that the scattering length within dental hard tissue[41] is not much longer than typical measured etch depths. (For this purpose we have assumed scattering within calculus to be comparable to that in enamel.) The same reasoning also predicts that increasing the incident fluence and corresponding etch depths effectively prevents stalling before complete removal of the calculus layer. These conclusions agree with our observations that stalling occurs close to the ablation threshold (1 to 2 J/cm^2) and is typically not observed for fluences >6 J/cm^2.

Of significant importance is the fact that sound cementum and enamel are not ablated below 9 and 12 J/cm^2, respectively.[42] Therefore, selective calculus ablation without stalling is assured for fluences of 6 to 8 J/cm^2.

Most ablation experiments in this study were carried out with gamma-ray–sterilized teeth. However, comparison of ablation rates of sterilized and unsterilized teeth under otherwise identical conditions were essentially indistinguishable. Previous NUV ablation studies[43] carried out at 380 nm reported ablation fluences of 1 to 2 J/cm^2 for effective calculus ablation using unsterilized teeth. Our comparison study eliminates the possibility that sterilization of the teeth significantly affects calculus ablation. We therefore suspect that the complicated nature of the temporal laser pulse shape in the 380-nm experiments (two successive, irregular 100-ns pulses within ~10 μs) may account for the different reported relevant ablation fluences.

Conclusion

Calculus ablation at 400 nm is best described by a modified blowoff model that is based on chromophore depletion (photobleaching). The results presented here strongly suggest that the relevant calculus chromophores are bacterial porphyrins, endogenous to plaque and dental calculus. A thin surface layer of these chromophores becomes photobleached after each irradiation pulse. Tissue scattering within this photobleached layer exacerbated by a decreasing absorber (bacterial porphyrin) density with depth leads to decreasing removal rates with successive laser pulses and potential ablation stalling. Stalling

can be avoided, however, by irradiating at incident fluences >6 J/cm^2.

REFERENCES

1. S. Jepsen *et al.*, Periodontol. 2000 **55**, 167 (2011).

2. S. Nyman *et al.*, J. Clin. Periodontol. **9**, 290 (1982).

3. P. Rechmann and T. Hennig, Med. Laser Appl. **16**, 223 (2001).

4. H. T. Bellini and J. R. Johansen, Acta Odontol. Scand. **31**, 283 (1973).

5. W. K. Brayer *et al.*, J. Periodontal. **60**, 67 (1989).

6. J. Eberhard *et al.*, J. Clin. Periodontol. **30**, 511 (2003).

7. A. Aoki *et al.*, Periodontol. 2000 **36**, 59 (2004).

8. A. M. Polson *et al.*, J. Periodontal. **55**, 443 (1984).

9. P. A. Adriaens *et al.*, J. Periodantal. **59**, 493 (1988).

10. L. J. Walsh, Aust. Dent. J. **48**, 146 (2003).

11. D. Fried, in *Photon Processing in Microelectronics and Photonics IV*, edited by J. Fieret *et al.* (SPIE, Bellingham, WA, 2005), Vol. 5713, pp. 259–269.

12. F. Schwarz *et al.*, J. Clin. Periodontol. **35**, 29 (2008).

13. F. Sgolastra *et al.*, Lasers Med. Sci. **27**, 661 (2012).

14. P. Rechmann, Dent. Clin. North Am. **48**, 1077 (2004).

15. P. Rechmann, T. Hennig, and B. Spengler, in *The 4th International Congress on Lasers in Dentistry*, edited by H. Loh (Monduzzi Editore, International Proceedings Division, Bologna, Italy, 1994), pp. 159–162.

16. P. Rechmann, U.S. Patent No. 5,795,153 (18 August 1998).

17. T. E. Bramanti and S. C. Holt, J. Bacteriol. **173**, 7330 (1991).

18. J. E. Schoenly, W. Seka, and P. Rechmann, Lasers Surg. Med. **42**, 51 (2010).

19. J. E. Schoenly, W. D. Seka, and P. Rechmann, J. Biomed. Opt. **16**, 071404 (2011).

20. J. E. Schoenly, W. Seka, and P. Rechmann, in *Lasers in Dentistry XVI*, edited by P. Rechmann and D. Fried (SPIE, Bellingham, WA, 2010), Vol. 7549, p. 754906.

21. J. E. Schoenly, W. Seka, J. D. B. Featherstone, and P. Rechmann, Lasers Surg. Med. **44**, 339 (2012).

22. A. Vogel and V. Venugopalan, Chem. Rev. **103**, 577 (2003).

23. G. H. Pettit, in *Lasers in Medicine*, edited by R. W. Waynant (CRC Press, Boca Raton, FL, 2002), pp. 109–133.

24. R. Srinivasan, Science **234**, 559 (1986).

25. G. H. Pettit *et al.*, Appl. Phys. A **58**, 573 (1994).

26. W. Buchalla, A. M. Lennon, and T. Attin, J. Periodontal. Res. **39**, 327 (2004).

27. Y. L. Qin *et al.*, J. Photochem. Photobiol. B:Biol. **87**, 88 (2007).

28. W. C. Dolowy *et al.*, J. Vet. Dent. **12**, 105 (1995).

29. B. T. K. Tan *et al.*, J. Periodontal. **75**, 23 (2004).

30. H. E. Schroeder, Helv. Odont. Acta **8**, 117 (1964).

31. J. Friskopp and L. Hammarström, J. Periodontal. **51**, 553 (1980).

32. J. Friskopp, J. Periodontal. **54**, 542 (1983).

33. J. R. Taylor, *An Introduction to Error Analysis: The Study of Uncertainties in Physical Measurements*, Second ed., Third print (University Science Books, Sausalito, CA, 1997), p. 327.

34. P. Rechmann and T. Hennig, in *Medical Applications of Lasers III*, edited by S. G. Bown *et al.* (SPIE, Bellingham, WA, 1996), Vol. 2623, pp. 180–188.

35. D. J. White, Biofouling **4**, 209 (1991).

36. P. Marsh and M. Martin, *Oral Microbiology*, 4th ed. (Oxford, Boston, MA, 1999), p. 193.

37. L. J. Walsh and F. Shakibaie, Australas. Dent. Prac. **18**, 56 (2007).

38. N. S. Soukos *et al.*, Antimicrob. Agents Chemother. **49**, 1391 (2005).

39. S. S. Socransky *et al.*, J. Clin. Periodontol. **25**, 134 (1998).

40. W. E. C. Moore and L. V. H. Moore, Periodontol. 2000 **5**, 66 (1994).

41. D. Fried, R. E. Glena, J. D. B. Featherstone, and W. Seka, Appl. Opt. **34**, 1278 (1995).

42. J. E. Schoenly, "Selective Ablation of Dental Calculus at 400 nm," Ph.D. thesis, University of Rochester, 2012.

43. P. Rechmann and T. Hennig, in *Lasers in Dentistry*, edited by H. A. Wigdor, J. D. Featherstone, and J. M White (SPIE, Bellingham, WA, 1995), Vol. 2394, pp. 203–210.